JCTC Journal of Chemical Theory and Computation

pubs.acs.org/JCTC Article

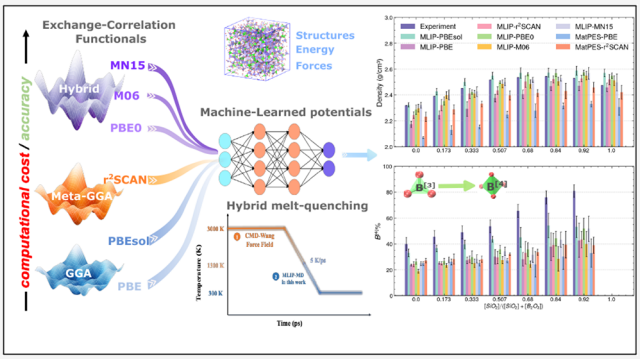
Influence of Exchange–Correlation Functional on Machine-Learned Interatomic Potentials' Accuracy: A Systematic Study of Borosilicate Glasses

Fengming Shi, Luca Brugnoli, and François-Xavier Coudert*

Cite This: J. Chem. Theory Comput. 2026, 22, 10961–10976 Read Online

ACCESS | Metrics & More | Article Recommendations | Supporting Information

ABSTRACT: Machine-learned interatomic potentials (MLIPs) have emerged as a strategy to accelerate molecular simulations, offering the promise of quantum chemical accuracy at a cost close to that of classical force fields. They are commonly trained on reference data obtained at the DFT level, which is itself a sufficiently affordable method to generate thousands of configurations and associated energies and atomic forces. However, this approach suffers from a major underlying challenge, which is rarely addressed: the choice of exchange–correlation functional. Although it is understood to have a crucial impact on the accuracy of the description of interactions and therefore on the results of the molecular simulations, it has not been systematically evaluated in the past. To go beyond simple benchmarks on selected configurations, we set out to understand the influence of exchange–correlation (XC) functionals on the training of MLIPs and, more importantly, on the physical properties of the resulting condensed matter systems. As a complex chemical system to test this, we selected borosilicate glasses of a wide variety of compositions. We produced reference data sets of borosilicate glasses with ten different chemical compositions, with six different XC functionals at the GGA, meta-GGA, and hybrid levels. We then trained MLIPs for all of them, produced glasses by melt-quenching, and compared their physical and structural properties with available experimental data. We show that there are significant differences between the different functionals. While the influence on bulk properties such as glass densities is minor, fine structural properties are more sensitive to the choice of functional, in particular when it comes to the coordination of boron atoms. Our results show how MLIPs can help us better understand the strengths and weaknesses of DFT functionals, where investigation through direct *ab initio* molecular dynamics was too expensive in the past. This also highlights that MLIPs depend on the ground truth on which they are trained, a fact often overlooked in practice, and this influence may be drastic for specific physical properties.

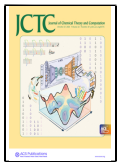


INTRODUCTION

Borosilicate glasses have been widely used in various applications, including some as diverse as laboratory glassware,[1] liquid-crystal screens,[2] and radioactive waste disposal[3] due to their high thermal stability and chemical durability. Borosilicate glasses are typically composed of multiple inorganic oxides where silica (SiO_2) and boron oxide (B_2O_3) mainly form the network backbone by covalent bonds, while alkali or alkaline-earth oxides, such as sodium oxide (Na_2O) and calcium oxide (CaO), typically modify the network structure.[4] Structurally, pure SiO_2 and B_2O_3 glasses consist of tetrahedral SiO_4 units and triangular BO_3 units, respectively, connected by bridging oxygen atoms. The addition of alkali or alkaline-earth cations leads to two competing mechanisms: on the one hand, serving as network modifiers to break covalent interconnections and create non-bridging oxygen atoms; on the other hand, acting as charge compensators to convert boron atoms from trigonal planar BO_3 units (hereafter denoted as $B^{[3]}$) to tetrahedral BO_4 units ($B^{[4]}$). The structural modification results in a nonlinear relationship between composition and physical properties, known as the boron anomaly,[5] posing significant challenges in accurately modeling the system.

Molecular dynamics simulations are among the primary techniques, alongside experimental measurements, for studying composition–structure–property relationships. Classical molecular dynamics (CMD) simulations have been widely used to investigate glasses,[6−9] and several empirical force fields (FFs) have been developed for borate or borosilicate glasses over the

Received: August 6, 2026
Revised: September 23, 2026
Accepted: September 24, 2026
Published: October 7, 2026



ACS Publications © 2026 The Authors. Published by American Chemical Society

past decades, categorized into rigid ionic models and polarizable interatomic models.[10] Early rigid ionic models are characterized by two-body energy terms based on the Born−Mayer−Huggins (BMH) potential, consisting of a Buckingham short-range interaction and a Coulombic long-range interaction. A few years ago, a more accurate FF was proposed by taking explicitly into account atomic charges and boron-related parameters as a function of composition,[11] encoding the variation of boron coordination as a function of composition for sodium borosilicate glasses, but showing a performance degradation at higher sodium compositions. Afterward, Deng and Du[12] extended this FF to aluminum-containing glasses. To improve the transferability of Kieu's potential, Wang et al.[13] developed an empirical interatomic potential for sodium−calcium borosilicate glasses based on the Guillot and Sator[14] potential by incorporating fixed partial charges and energy terms related to boron element. This allowed a good reproduction of density and $B^{[4]}$, but the FF underestimated the density with respect to experiments in practical scenarios.[15] Lately, Sundararaman et al.[16−18] proposed a pairwise interatomic potential, where the partial charge of oxygen was composition-dependent, by evaluating the long-range Coulombic interactions using Wolf truncation. On the other hand, to explicitly consider polarization effects, charge redistribution, and bond breaking, some researchers dedicated themselves to the development of polarizable interatomic models. For instance, the core-shell model,[19] polarizable ion model[7] and BMP model,[20,21] exhibit good agreement with experiments for selected properties. However, their applications have been limited due to the complex nature and the resultant low transferability.

Even from this very cursory review, it is clear that a vast array of empirical force fields exists for borosilicate glasses and that there is no silver bullet, i.e., a universal, transferable, and accurate solution. In comparison, *ab initio* molecular dynamics (AIMD) provides higher accuracy for the calculation of energies and atomic forces based on the density functional theory (DFT). However, it has a much larger computational cost, which limits its application mainly to small system sizes and short-timescale simulations. Therefore, it is unfavorable for glass simulations, particularly for complex multicomponent systems or at low quenching rates.[19,22−24]

As a compromise between these two levels of theory, machine-learned interatomic potentials (MLIPs) have seen very rapid adoption in chemical and material sciences.[25−27] MLIPs can achieve DFT-level accuracy while maintaining computational efficiency close to that of classical MD. They reproduce the potential energy surface (PES) of atomic systems by learning from energies and atomic forces, enabling the simulation of longer time scales and larger system sizes than were previously possible through AIMD. In recent years, MLIPs have been used in glass simulations including single-component[28−30] and multicomponent[31−36] oxides, but only a few studies have dealt with borosilicate glasses. Urata's group employed an MLIP to investigate superstructures like boroxol rings that some FFs failed to capture in sodium borate[33] and lithium borate glasses;[34] they then updated the model by enlarging the DFT datasets for lithium borosilicate glasses.[35] The results demonstrated that the revised MLIP achieved good accuracy in density and short-range and medium-range order structures but underestimated the ratio of $B^{[4]}$ (denoted as $B^{[4]}$%) relative to experiments. Similarly, superstructures have been reproduced using MLIPs for five-component oxide glasses developed by Kayano et al.,[36] whose potential exhibited good accuracy in density and $B^{[4]}$% prediction for multicomponent glasses with discrepancies of 0.06 g/cm^3 and 10% compared to experiments, respectively. It should be noted that although most of the physical and structural properties calculated by these MLIPs were in good agreement with experiments, they consistently underestimated the prediction of $B^{[4]}$%, a critical descriptor for B_2O_3-containing glasses. This underestimation is not only affected by the molecular dynamics settings especially the quenching rates and system sizes but also inherently restrained by the accuracy of MLIPs, which depends on the quality of the training datasets.

Although DFT-based data are predominantly used for the construction of reference data sets for condensed matter systems, DFT represents a diverse family of quantum chemistry methods, with many different choices affecting the accuracy of the atomic forces, the first of which is the XC functional. For example, Morawietz et al.[37] demonstrated that MLIPs trained on different XC functionals can yield substantially different predictions of the dynamic properties of water. However, studies comparing the various common choices of XC functionals for MLIPs are often focused on small benchmarks and specific properties. In this work, we systematically investigated the influence of six XC functionals (including GGA, meta-GGA, and hybrid functionals) on the performance of MLIPs in reproducing the physical and structural properties of sodium−calcium borosilicate glasses. We put particular focus on the impact of XC functionals on physical properties such as glass density and $B^{[4]}$%, as well as local atomic environments. In this way, through melt-quench simulations, we used the differently trained MLIPs as a proxy to investigate the accuracy of the DFT functionals themselves on this complex family of systems with varying chemical compositions. Our results show how MLIPs can help us better understand the strengths and weaknesses of DFT functionals, where investigation through direct *ab initio* molecular dynamics has been too expensive in the past. It also highlights that MLIPs depend on the ground truth on which they are trained, a fact often overlooked in practice, and this influence may be drastic for specific physical properties.

SYSTEMS AND METHODS

In this section, we describe the nature and composition of the borosilicate glass systems that we studied, details regarding the construction of reference datasets (including the DFT methodology, choice of exchange−correlation functionals, etc.), the methodological choices for training MACE interatomic potentials, and the proposed melt-quenching protocol.

Construction of Reference Datasets

In this study, we focused mainly on a series of soda-lime borosilicate glasses with varying chemical composition. In order to investigate a broad range of SiO_2:B_2O_3 ratios, we studied glasses with the following compositions: $(75 - x)SiO_2 \cdot xB_2O_3 \cdot 15Na_2O \cdot 10CaO$, where x = 0, 6, 12, 24, 37, 50, 62, and 75. These structures have been experimentally investigated by Smedskjaer et al.[38,39] allowing for a detailed comparison of the computed properties. Additionally, we also studied a glass composition (named "10B") with increased CaO content—which we considered as a verification composition to evaluate the final performance of the interatomic potentials, since its structure was experimentally characterized by neutron

https://doi.org/10.1021/acs.jctc.6c01609
J. Chem. Theory Comput. 2026, 22, 10961−10976

diffraction.[40] All compositions studied and experimental data available are summarized in Table 1. Pure SiO_2 and B_2O_3 were also included in the reference datasets.

Table 1. Compositions and Properties of the Investigated Borosilicate Glasses and Their Associated Experimental Properties: Density, Proportion of Four-Coordinated Boron Atoms, and Glass Transition Temperature T_g[38−40]

	Chemical composition (mol %)						
Glass ID	SiO_2	B_2O_3	Na_2O	CaO	Density (g/cm^3)	$B^{[4]}$ (atomic %)	T_g (K)
75B	0	75	15	10	2.344	39.9	775
62B	13	62	15	10	2.417	45.3	790
50B	25	50	15	10	2.490	48.9	803
37B	38	37	15	10	2.539	53.5	813
24B	51	24	15	10	2.581	65.5	833
12B	63	12	15	10	2.587	75.8	842
6B	69	6	15	10	2.570	80.8	837
0B	75	0	15	10	2.530	n/a	814
10B	60	10	15	15	2.620	70.0	798

The computational workflow is shown in Figure 1; first, we prepared the initial structures of each composition using classical molecular dynamics (CMD) according to the protocol in the following section. Second, the reference datasets were sampled from molecular dynamics trajectories in the (N, V, T) ensemble, using both *ab initio* and classical MD. We sampled 3000 structures from AIMD at T = 2500 K, with cell parameters varied from the experimental densities by −1.5%, 0%, and +1.5%, and an additional 3000 structures from CMD at T = 300, 1500, and 2000 K to improve the diversity of the configurational space. Thirdly, for all of the structures, the total energy and atomic forces were computed by DFT single-point calculations using six different XC functionals (PBE,[41] PBEsol,[42] r^{2}SCAN,[43] PBE0,[44] M06,[45] and MN15[46]) as implemented in CP2K software.[47] The respective datasets are denoted as D-PBE, D-PBEsol, D-r^{2}SCAN, D-PBE0, D-M06, and D-MN15 for convenience. Each reference dataset was randomly split into three parts including a training set, a validation set, and a test set, in the proportion 8:1:1. Finally, the MACE model was fitted to the training set and checked on the validation set to optimize model hyperparameters. The final performance of the trained model was measured on the test set, which was completely unseen data before this final performance evaluation. The details of the methods involved are given in the following sections.

Classical Force Fields

Classical molecular dynamics (CMD) simulations were used in two different ways. First, to generate glassy structures of borosilicate compositions (see Table 1), which served as starting points for structure sampling and AIMD at 2500 K. Second, CMD was combined with MLIP-MD to perform a hybrid melt-quench protocol. We used the empirical force field for borosilicate glasses developed by Wang et al.[13] (termed CMD-Wang).

The initial random structures for each composition were generated by random placement of atoms in a cubic simulation box, whose size was determined according to the experimental density. Periodic boundary conditions were applied in all directions. The total number of formula units of the borosilicate glasses for each composition was set to 100, leading to between 300 and 500 atoms in each structure. Such a system size has been established as sufficient to represent the physical properties of borosilicate glasses.[33] From these random structures, classical MD simulations were performed with LAMMPS software.[48] The cutoff values for short-range interactions were set to 11 Å. The long-range part of the Coulombic interactions was calculated using the Ewald algorithm with an accuracy of 10^{-4}. The MD time step was fixed at 1 fs. The initial structures were simulated using the standard melt-quench procedure as shown in Figure 1(a). The system was melted at 3000 K in the (N, V, T) ensemble for 10 ps and in the (N, P, T) ensemble at zero pressure for 100 ps. Subsequently, a linear cooling procedure with a rate of 1 K/ps was applied to the system under (N, P, T) conditions until the

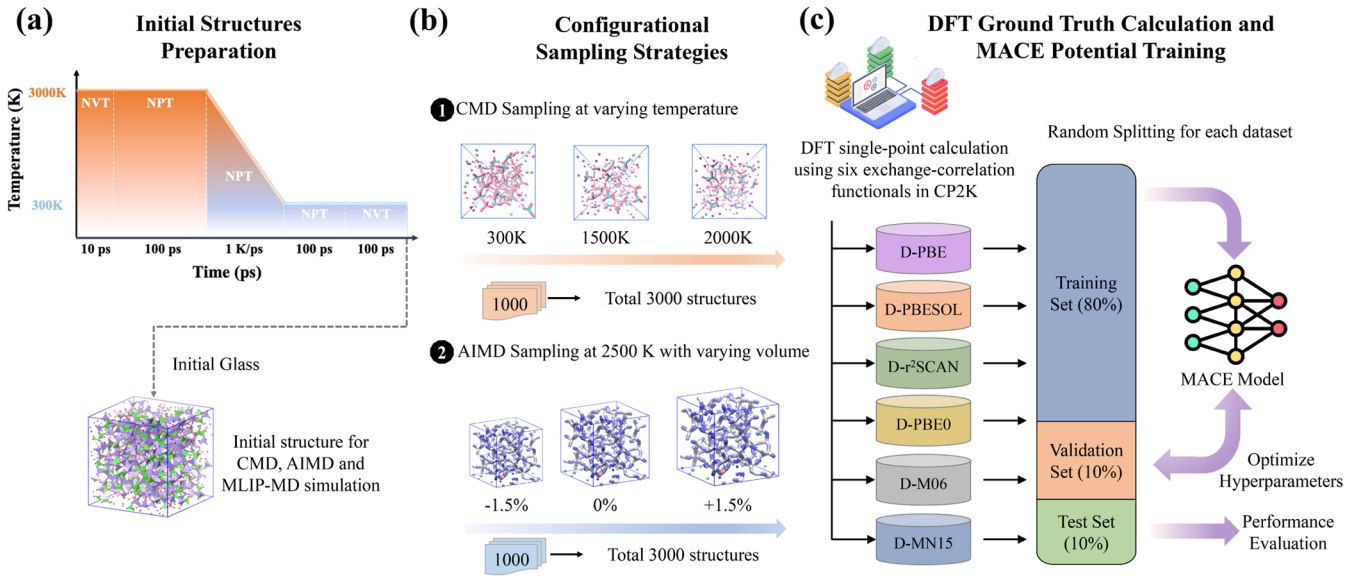


Figure 1. Schematic representation of the computational workflow adopted in this work, including: (a) preparation of initial structures, (b) sampling of configurations, and (c) DFT ground truth calculations and training of MACE interatomic potentials.

https://doi.org/10.1021/acs.jctc.6c01609
J. Chem. Theory Comput. 2026, 22, 10961−10976

temperature reached 300 K. All of the glasses were further relaxed at 300 K and zero pressure for 100 ps in the (N, P, T) ensemble, followed by an (N, V, T) equilibration process for 100 ps.

As shown in Figure 1(b), half of the structures were sampled from molecular dynamics trajectories generated using CMD-Wang according to the following protocol. The initial structures thus prepared were heated at a rate of 1 K/ps in (N, V, T) to different temperatures (300, 1500, and 2000 K) and held at these temperatures in (N, V, T) for 200 ps. For each trajectory, 100 structures per temperature were extracted from the last 100 ps at an interval of 1 ps for DFT single-point calculations, leading to 3000 structures in total.

DFT Calculations

The reference data sets for energies and atomic forces of borosilicate glass configurations were obtained through DFT calculations with various XC functionals (as will be detailed in the next section). We also used DFT calculations as part of our high-temperature *ab initio* MD simulations to sample the potential energy surface of the system and generate configurations—as sampling structures at high temperature ensures more diversity in configurational space and wider energy ranges.[25] AIMD simulations for all compositions were performed from initial structures (generated by CMD) using Quickstep/CP2K software.[47,49] This package takes full advantage of the hybrid Gaussian and plane-wave (GPW) method and its augmented extension (GAPW), where the wave function is described with an atom-centered Gaussian-type basis, and the electron density is described with an auxiliary plane-wave basis.[50] To reduce the number of explicit electrons, the inner cores of all elements (Si, B, O, Ca, Na) were replaced by the use of Goedecker−Teter−Hutter (GTH) pseudopotentials[51−53] generated specifically for the SCAN functional (GTH-SCAN). We used triple-ζ valence-polarized Gaussian basis sets. The SCF convergence threshold was set at 8×10^{-7} Hartree with a cutoff of 900 Ry and a relative cutoff of 50 Ry. For the AIMD simulations, we relied on the r^{2}SCAN XC functional.[43] We used the DFT-D3 dispersion correction, with Becke−Johnson damping (BJ), C_9 terms, and a cutoff of 15 Å.[54]

To increase the diversity of the configurational space sampled, the unit cells of the starting structures were varied by −1.5%, 0%, and +1.5% for each composition. Born−Oppenheimer MD simulations with a time step of 0.5 fs were carried out in the (N, V, T) ensemble at 2500 K, using a CSVR thermostat[55] with a time constant of 150 fs. Each system was simulated for a duration of 10 ps, and for each trajectory, 100 snapshots were sampled, leading to 3000 structures.

To compare the influence of XC functionals on the resulting MLIPs, the energies and forces of the 6000 configurations sampled from both AIMD and CMD trajectories were recalculated using DFT single-point calculations with all six chosen functionals. In these DFT calculations, dispersion interactions were included, using the DFT-D3 (BJ) dispersion correction, C_9 terms, and a cutoff of 15 Å. In addition, the isolated atomic reference energies required for MACE training were then calculated by placing each atom (Si, B, O, Ca, and Na) in a cubic cell with a lattice parameter of 20 Å using nonperiodic boundary conditions. The six representative XC functionals, along with the corresponding pseudopotentials, grid cutoff, and relative cutoff, are detailed in the following section.

Exchange−Correlation Functionals

In order to study the influence of exchange−correlation functionals on the MLIPs and the glass properties, we chose to include PBE[41] and PBEsol[42] as GGA-level functionals because of their wide usage for data generation in condensed-matter systems like glasses. At the meta-GGA level, we decided to employ the r^{2}SCAN[43] functional, because of its good balance between accuracy and numerical efficiency (in particular compared to SCAN). Among various hybrid functionals, we have selected PBE0[44] for our study, as it is one of the most widely used hybrid functionals for condensed-matter systems and has been applied in particular to glass systems.[56−58]

Finally, we added two hybrid Minnesota-family functionals MN15[46] and M06[45] to our shortlist of XC functionals. MN15, a combination of 44% Hartree−Fock exchange with the meta-NGA MN15-L,[59] is mainly designed for broad accuracy for main-group and transition-metal chemistry, showing great performance for the description of bond distances and noncovalent interactions. Theoretically, it has great promise in accurately describing the local environments of boron atoms and capturing changes in boron coordination and was included in our selection. Furthermore, MN15 was incorporated specifically to serve as a stress test for the influence of high Hartree−Fock exchange. M06, similarly developed for broad accuracy across main-group and transition-metal chemistry, is a global hybrid meta-GGA functional with 27% Hartree−Fock exchange. The inclusion of M06, which belongs to the same Minnesota family as MN15 but developed with a different functional form, parameters, and fraction of exact exchange, allows us to examine whether the behavior observed in MN15 is specific to this functional or reflects a more general characteristic of Minnesota-family functionals in borosilicate glasses. In total, our six XC functionals selected are PBE, PBEsol, r^{2}SCAN, PBE0, M06, and MN15.

The choice of many technical settings in DFT calculations, in particular when hybrid functionals are involved, plays a significant role in obtaining accurate results. CP2K uses a multigrid approach, using four grid levels by default. The plane-wave cutoff and the relative cutoff for each XC functional were determined by convergence tests with a strict criterion of 10^{-10} Ry in the total energy. Based on these tests, the cutoffs for PBE, PBEsol, r^{2}SCAN, PBE0, M06, and MN15 were set to 1000, 1000, 1200, 1000, 1000, and 1000 Ry, respectively, with corresponding relative cutoffs of 100, 80, 100, 100, 90, and 100 Ry. For a total of 399 structures (approximately 1.1% of the 36000 structures, corresponding to 6000 unique structures evaluated using six different exchange-correlation functionals) that initially failed to converge in the SCF calculation, the cutoff and relative cutoff were increased to 1200 and 100 Ry, respectively. Structures that still did not converge were discarded, leaving 5893 configurations common to all six datasets.

As for the pseudopotentials, we used GTH-SCAN for r^{2}SCAN functional and GTH-PBE for the remaining XC functionals. Moreover, the truncated Coulomb operator and the auxiliary density matrix method (ADMM) were employed to reduce the computational cost of hybrid functionals. The truncation radius was set to 7 Å, and the admm-tzp was chosen as the auxiliary basis set. All hybrid-functional single-point calculations were initialized using the wavefunctions obtained from PBE single-point calculations. The complete settings for the DFT single-point calculations are summarized in Table S1.

https://doi.org/10.1021/acs.jctc.6c01609
J. Chem. Theory Comput. 2026, 22, 10961−10976

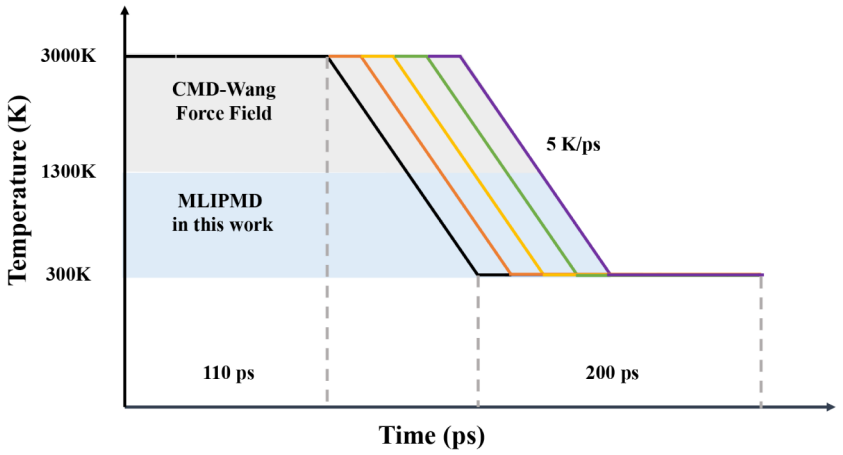


Figure 2. Schematic representation of the hybrid melt-quench protocol developed in this work and used to simulate borosilicate glasses, using a combination of classical molecular dynamics (CMD-Wang, based on the force field of Wang et al.[13]) and MLIP-based molecular dynamics (MLIP-MD). The different colors represent independent simulations.

MLIP Training

Using the training data set produced as explained above, we trained a machine-learned interatomic potential (MLIP) based on the MACE architecture.[60,61] MACE is grounded in a many-body equivariant message-passing neural network (MPNN) architecture featuring the physical symmetries of atomic structures, converging fast and more accurately, as well as supporting multi-GPU training. Therefore, these advantages make it a promising model for fitting the DFT reference datasets for borosilicate glasses. We trained a MACE model for each reference dataset, i.e., for each XC functional, and the model parameters were updated by minimizing the loss function defined as the weighted sum of the mean squared error of energy and force components on the training sets. Stresses were not taken into account in the training. As a test, we also trained and benchmarked an MLIP-PBEsol model based on energy, forces, and stresses. It showed good agreement with DFT (RMSE of 8 meV/atom, 54 meV/Å, and 33 meV/Å^3, respectively), but produced unstable (N, P, T) dynamics. This behavior is consistent with known challenges in using CP2K stress tensors from large disordered configurations at high temperatures as training targets.

The development of the MACE potential requires the choice of hyperparameters of the model, which determine the accuracy of the potential and its computational cost. As suggested by MACE developers, three model hyperparameters including `num_channels` (number of channels, determining the size of the model), `max_L` (symmetry of the messages), and `r_max` (cutoff radius for the local environment in each layer) were adjusted on the validation set in this work. The final model was trained with a cutoff radius of 6 Å, 128 tensor decomposition channels, and message passing symmetry of up to order 1. In addition to the model's hyperparameters, optimization parameters such as `forces_weight` and `energy_weight` in the loss function that control the relative precision of energy and force predictions are critical for the MACE potential training, as atomic forces are local quantities that implicitly contain derivative information of the energy with respect to atomic positions. All MACE models were trained using a two-stage optimization procedure with early stopping based on the validation set. Therefore, in the first training stage, we prioritized accurate force predictions using a high ratio of `forces_weight` to `energy_weight`. After the forces converged, the second stage began with an increased energy penalty equal to that of the forces and a reduced learning rate, approximately starting from the final 20% of the training epochs. The training was terminated after the models converged when the validation performance showed no improvement for 50 consecutive epochs. The complete set of model parameters is provided in Table S2, and the training input files are made available.

Melt-Quench Protocol

The melt-quench approach is widely used to generate atomistic glass structures from molecular simulations, following *in silico* the same approach as is used experimentally, by heating the sample to the liquid state and then rapidly cooling it. The choice of cooling rate plays a drastic role in the structural features and physical properties of the final glasses, especially for boron-containing glasses where boron speciation and boroxol ring formation are strongly cooling-rate-sensitive,[62,63] and a more realistic (lower) cooling rate leads to a more accurate evaluation of the material properties from atomic simulations, but at the price of higher computational cost. Although they have lower cost than DFT calculations, MLIPs are still slower to evaluate than analytical classical force fields; therefore, we developed in this work a new "hybrid" melt-quench protocol to combine the best of empirical FFs and MLIPs.

Inspired by Erhard et al.,[29] we split the standard melt-quench process into two sections with different force fields. The key challenge is that the required FF must accurately describe the rearrangements of the internal structure of borosilicate glasses, especially during the glass transition. In contrast, a slightly less accurate but faster FF is sufficient for the heating and initial cooling stages, where the system remains in a very disordered, high-temperature liquid state.

The proposed melt-quench procedure is represented schematically in Figure 2. The initial structures are first melted through the use of a classical force field as described above. The high melting temperature ensures that the structural memory of the initial configuration is completely erased. The system is then cooled to 1300 K at a constant rate of 5 K/ps at zero pressure in the (N, P, T) ensemble. This cooling rate represents a good compromise between the use of more

https://doi.org/10.1021/acs.jctc.6c01609
J. Chem. Theory Comput. 2026, 22, 10961−10976

Table 2. Statistical Evaluation of the Six MLIPs Based on Different XC Functionals, Displaying the Mean Absolute Error (MAE) for Energy and Atomic Forces on Training, Validation, and Test Data Sets[a]

	Energy (meV/atom)			Force (meV/Å)		
Potentials	Training	Validation	Test	Training	Validation	Test
MLIP-PBE	0.84	0.82	0.82	38.24	39.33	40.04
MLIP-PBEsol	0.79	0.79	0.64	31.58	32.74	32.84
MLIP-r^{2}SCAN	0.45	0.58	0.42	29.84	31.79	31.75
MLIP-PBE0	0.85	0.81	0.75	35.08	36.20	36.60
MLIP-M06	0.94	0.81	0.75	94.24	94.73	95.11
MLIP-MN15	1.07	0.77	1.02	131.43	131.70	130.15

[a]The force errors are evaluated per Cartesian component in this work.

realistic cooling conditions and the computational cost. At this switching temperature, the systems are still in the liquid state and far from the glass transition temperature, as confirmed by experimental evidence[38] and the calculated mean-squared displacement (MSD) in Figure S1. The MLIP-MD then takes over the quenching process from 1300 to 300 K, following the same temperature ramp. Subsequently, the system is relaxed for 100 ps at 300 K and zero pressure using (N, P, T), followed by a (N, V, T) equilibration run of 100 ps for statistical averaging. Five independent simulations for each composition are restarted with different velocities by increasing the melting duration by 2 ps in the CMD. All of the physical and structural properties were calculated using five independent trajectories. In the MLIP-MD simulations, the LAMMPS code compiled with MACE support is used to carry out the hybrid melt-quench protocol, using the `mace` pair_style with the `mliap unified` parameter.

RESULTS AND DISCUSSION

In order to investigate the impact of the choice of DFT XC functional on the structural and physical properties of glasses at a scale that has not been achieved before, we created 6 data sets of reference configurations (along with energies and atomic forces) for 6 different DFT functionals: PBE, PBEsol, r^{2}SCAN, PBE0, M06, and MN15. On the basis of these data, we trained one MLIP to reproduce the DFT data of each functional and used them to simulate borosilicate glasses of different compositions. All molecular dynamics simulations were conducted using a newly proposed hybrid melt-quench protocol that combines empirical force fields with well-trained MLIPs (see Systems and Methods) to improve computational efficiency, and we analyze below the impact of the XC functional on the generated borosilicate glasses.

Training and Validation of MLIPs

Full details of the training of the 6 MLIPs for each XC functional studied are presented in Figures S2−S7. We plot the learning curves of the loss function, as well as the evolution of the mean absolute error (MAE) for energies and forces on the validation set, as a function of the number of epochs (i.e., the progress of the training).

We tested the generalization capabilities of the final trained MLIPs by evaluating them on unseen data sets. These results are shown in the form of parity plots of energies and atomic forces, depicted in Figures S8−S13, along with the respective MAE for each case. We note that the energies presented are the atomization energies (the total energy of the isolated atoms minus the total energy of a structure). All of the data points are located near the diagonal line of both atomization energies and forces, showing good consistency between predictions and DFT calculations, but such parity plots alone are not sufficient for a comprehensive statistical evaluation of the trained models.

To systematically assess the predictive ability of the six MLIPs, the MAEs of energies and atomic forces for the training, validation, and test sets are summarized in Table 2. On these three data sets, the MAEs of energies and forces are below 1 meV/atom and 40 meV/Å for the MLIPs trained on PBE, PBEsol, r^{2}SCAN, and PBE0, while the MAEs are approximately 1 meV/atom for energies and 95 meV/Å and 131 meV/Å for forces for the cases of the MLIPs trained on the M06 and MN15 functionals, respectively. Comparing the training and validation metrics, we can confirm that the MLIPs are generally well trained, with neither overfitting nor underfitting. However, it is clear that MLIP-MN15 and MLIP-M06 exhibit significantly higher MAEs for forces compared to the other models.

This is confirmed by visual inspection of the parity plots for the atomic forces, as shown in Figure S12 and Figure S13, where some of the data points are scattered far from the diagonal, especially for MLIP-MN15. There is no reason for the M06 and MN15 potential energy surfaces of the system to be intrinsically harder to learn, or to state it in another way, for MLIP-M06 and MLIP-MN15 to underperform compared to other models, with all model hyperparameters being otherwise carefully tuned. Therefore, we can attribute this low performance to noise (i.e., high variance) in the DFT data for the M06 and MN15 functionals. Moreover, by inspecting the atomic forces for each composition individually (Figure S14 and Figure S15), we find that this noise is not present in systems containing only SiO_2 or B_2O_3, but is only seen in compositions including Na_2O. To identify the origin of the larger force errors, we decomposed the composition-based force errors into element-based force errors reported on identical structures across the six data sets in Table S4. The MAEs of the atomic forces for Na are 0.259 and 0.863 eV/Å for MLIP-M06 and MLIP-MN15, respectively, notably higher than those for other elements. The results show that the higher force errors of MLIP-MN15 and MLIP-M06 are directly associated with the presence of Na in the system.

Comparison of Exchange−Correlation Functionals

To further investigate the impact of XC functionals on the atomic forces, which are the primary information used in MLIP-based MD simulations, we have analyzed the relationships among them across the 5893 common configurations in the six DFT datasets. We show in Figure 3 (in heatmap form) the mean absolute error in forces between any two pairs of XC functionals. This gives us an estimate of how "far" two XC functionals are from each other, in the space of atomic forces.

https://doi.org/10.1021/acs.jctc.6c01609
J. Chem. Theory Comput. 2026, 22, 10961−10976

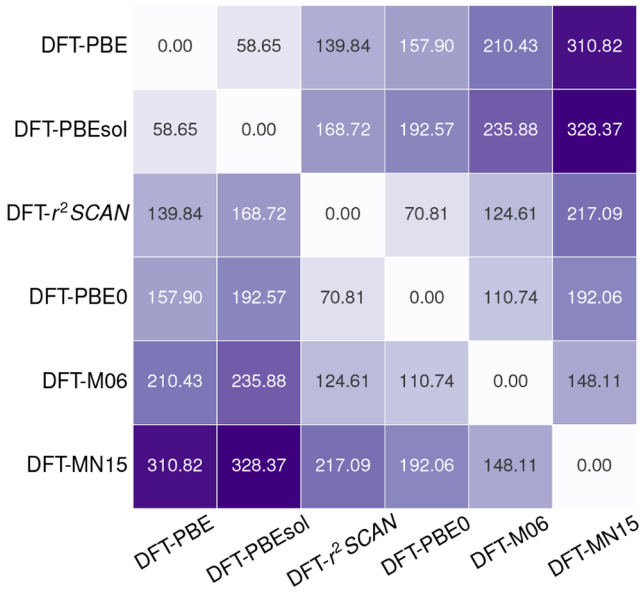


Figure 3. Mean absolute error (MAE) of the atomic forces for common structures across different DFT XC functionals (in meV/Å).

We clearly observe a strong similarity between functionals of the same level of theory, such as PBE and PBEsol (with an MAE of 59 meV/Å), or between the hybrid PBE0 and the meta-GGA r^{2}SCAN (71 meV/Å). The MAEs across these families are higher, ranging between 140 and 193 meV/Å. In contrast, the force differences between these functionals and the two Minnesota functionals are generally larger. M06 shows an MAE of forces spanning 111 to 236 meV/Å compared to other functionals, while MN15 exhibits higher force differences ranging from 148 to 329 meV/Å. These results indicate that the Minnesota functionals, especially MN15, produce systematic differences in potential energy surfaces compared to the other functionals involved here, suggesting that the larger force errors in the corresponding MLIPs observed mostly originate from functional variations in the underlying DFT data sets.

Additionally, these results highlight why r^{2}SCAN is a common choice for sampling potential energy surfaces and generating DFT data sets for training MLIPs: it is close to the accuracy of the hybrid XC functional PBE0, while being computationally less demanding. We find on our data set that r^{2}SCAN is 42% faster than PBE0 on average; see Table S3 for a summary of the computational cost for all functionals studied.

Finally, we note that the force error of each MLIP is smaller than the smallest difference between its reference functional and the other functionals, even for the closest ones like PBE and PBEsol. This confirms that our MLIPs trained on DFT data achieve good chemical accuracy, as they are able to capture not only the generic features of the potential energy surface of the system across compositions, but also the finer distinctions between XC functionals. We also note that, while MLIP-MN15 shows lower accuracy than MLIPs based on other XC functionals in this work, it still achieves reasonable accuracy compared to other MLIPs reported in the field of borosilicate glasses, with an MAE of 130 meV/Å in the present work, compared to 154 meV/Å in ref 36 and 203 meV/Å in ref 32.

Cross-Functional Consistency Analysis

The comparison of DFT forces performed above indicates that MLIPs can theoretically resolve differences among XC functionals. In this section, we investigate whether our MLIPs preserve the relative ordering of these functionals and

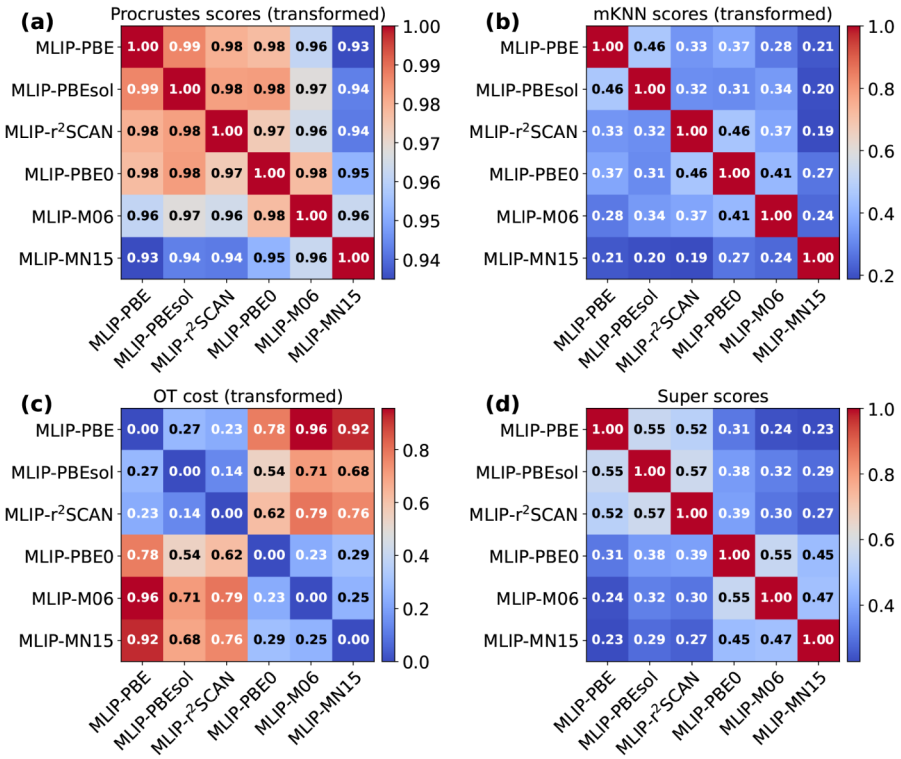


Figure 4. Model similarity as evaluated by (a) Procrustes scores (global alignment); (b) mKNN scores (local fidelity); (c) normalized OT cost; and (d) the composite SuperScore (see text for details). Color bars indicate the magnitude of each metric.

https://doi.org/10.1021/acs.jctc.6c01609
J. Chem. Theory Comput. 2026, 22, 10961−10976

capture the magnitude of their differences by exploring the latent representations of the MLIPs and comparing the relative energy and force differences between each pair of functionals at the MLIP and DFT levels on the identical structures.

Latent Representations of the XC-Functional Hierarchy. We employ a latent representation framework recently proposed by Li and Walsh[64] to quantify the similarity of learned latent representations across the six MLIPs in our work. The atomic embeddings of each model are extracted from the first interaction layer of the MACE model, and then they are projected into a unified representation space, defined by 100 anchors selected from MLIP-PBE using the DIRECT method,[65] aiming at filtering out the influence of training settings in different models. The transformed representations for each model are projected onto a two-dimensional principal component analysis (PCA) space, as shown in Figure S16. We observe that the positions and distributions of the five elements in the borosilicate glasses exhibit highly similar latent representations in the global manifold across all models. Furthermore, the local latent representations are visualized using boron as an example by mapping the aligned boron embedding onto properties including boron coordination and the B−O bond length, as shown in Figure S17. The MLIPs trained with different XC functionals show distinct local organizations of the boron representations in relative positions and distributions with MLIP-MN15 showing particular differences. In addition, some common features exist across the MLIPs. First, $B^{[3]}$- and $B^{[4]}$-dominated regions can be observed in each latent representation rather than distributed randomly. Second, the B−O distance variation can be observed across the latent representation space with the $B^{[3]}$ and $B^{[4]}$ dominated regions presenting distinct but partially overlapping B−O distance distributions. These observations suggest that the MLIPs both preserve the XC-functional differences in local representations of atomic embeddings and encode the chemical information in a physically meaningful manner.

The latent representations are quantitatively evaluated by four metrics that encompass three key aspects including the global topological manifold, the local atomic environment, and the atomic embedding distance distribution. The Procrustes score measures the global similarity in terms of chemical space organization between two models.[66] The mutual k-nearest neighbors (mKNN) score evaluates the local similarity by computing the fraction of common nearest neighbors for the same atomic embeddings. The normalized optimal transport (OT) score measures the distance distribution of transformed atomic embeddings in the unified space, simultaneously characterizing the global and local differences.[67] Additionally, a combined metric (Super score, $\text{SuperScore} = \frac{1}{2}(\text{Score}_{\text{Procrustes}} + \text{Score}_{\text{mKNN}}) \times e^{-\text{Score}_{\text{OT}}}$) is defined by averaging the global and local scores and penalizing the transport cost, providing a comprehensive evaluation of representational similarity for MLIPs.[64] This serves as an overall indicator to examine whether the MLIPs preserve the relative ordering of XC functionals. The results of all metrics are shown in Figure 4.

In panel (a), we see that all MLIP pairs exhibit remarkably high global topological similarity (Procrustes scores of >0.90). Conversely, local neighborhood similarity remains at a low level (as seen in panel (b)), basically dropping from MLIPs trained on GGA to hybrid functionals. This indicates that, although MLIPs eventually converge to a consistent global manifold, their local atomic representations remain different. The OT cost scores roughly separate the six models into two tiers (in panel (c)). For example, transforming the distance distribution of MLIP-PBE into those of MLIP-M06 and MLIP-MN15 needs a much higher cost than transforming it into those of MLIP-PBE0, MLIP-r^{2}SCAN, and MLIP-PBEsol. This is consistent with the theoretical complexity and hierarchy of XC functionals. This relative ordering is further evidenced by the superscores in panel (d), where the similarity between MLIP-PBE and other MLIPs decreases sequentially from 0.55 (MLIP-PBEsol) to 0.23 (MLIP-MN15). Therefore, we conclude that MLIPs effectively capture and preserve the relative hierarchical ordering of the underlying XC functionals.

Preservation of XC-Functional Differences. In this section, we investigate whether MLIPs are capable of resolving subtle differences between XC functionals by comparing pairwise energy and force differences between the DFT reference calculations and the corresponding MLIP predictions. For the two functionals, PBE and PBEsol, we define the energy difference for each configuration as $\Delta E_{\text{DFT}} = E_{\text{DFT}}^{\text{PBE}} - E_{\text{DFT}}^{\text{PBEsol}}$, with the corresponding MLIP quantity defined similarly. For forces, we compare the mean absolute force difference (MAFD) between each pair of functionals in Cartesian components at the DFT and MLIP levels. The Pearson correlation coefficient is used to measure the correlation of pairwise functional differences obtained from the DFT calculations and those predicted by the corresponding MLIPs. The parity plots of pairwise functional energy differences are shown in Figure S18, while the corresponding results for force differences are presented in Figure S19.

For energy differences, the DFT and corresponding MLIP results show excellent agreement across all pairs of functionals, with Pearson correlation coefficients greater than 0.99. This indicates that the MLIPs faithfully preserve the relative energetic differences between various functionals. Conversely, the consistency of force differences varies, depending on the functional pairs. For PBE, PBEsol, PBE0, and r^{2}SCAN, the majority of data points are linearly distributed along the diagonal, with Pearson correlation coefficients greater than 0.6. For the M06- and MN15-containing functional pairs, a large fraction of data points deviate from the diagonal, consistent with our previous analysis. This can be mainly attributed to the larger Na-related force errors observed in the resulting fitted MLIPs for M06 and MN15, reducing the agreement of MAFD between functionals at the DFT level and in the corresponding MLIPs. This interpretation is further supported by the substantial reduction in the force deviations in pairwise MAFD for M06- and MN15-containing functional pairs when the Na-related contribution is excluded (Figure S20). This indicates that the MLIPs can retain the relative force differences between functionals to a substantial extent, while their quantitative reproduction is limited by the precision for Na in DFT and in the corresponding MLIPs.

Overall, these results demonstrate that the MLIPs are capable of preserving the relative differences between XC functionals, while their fidelity depends on the magnitude of differences in functional-based DFT and on the accuracy of individual MLIPs.

Impact of Exchange−Correlation Functional on Glass Properties

In order to study the impact of the choice of XC functionals on the properties of borosilicate glasses, we have used each MLIP

https://doi.org/10.1021/acs.jctc.6c01609
J. Chem. Theory Comput. 2026, 22, 10961−10976

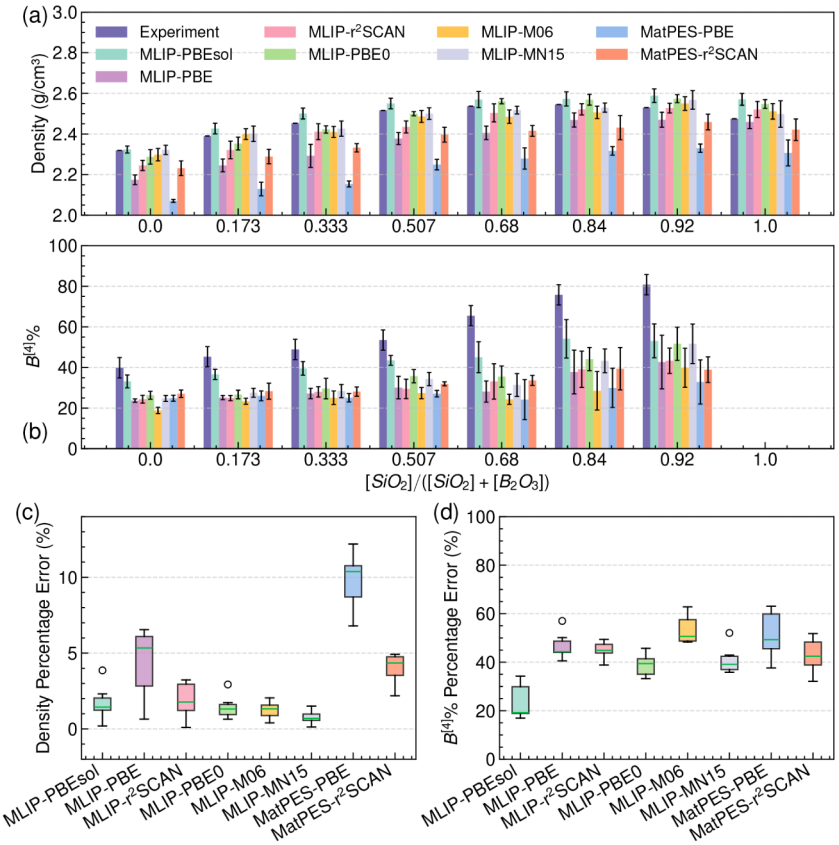


Figure 5. (a) Density and (b) $B^{[4]}$% statistics of borosilicate glasses using MLIP-MD built on different XC functional reference datasets and MACE foundation models, and box plots of the corresponding relative error in (c) density and (d) $B^{[4]}$%.

to produce glass models through a melt-quench protocol (summarized in Figure 2) and to characterize various physical properties of these glasses. Among these, glass density is easy to measure experimentally and therefore commonly used to evaluate the accuracy of force fields. Moreover, for borosilicate glasses, the evolution of boron coordination (between $B^{[3]}$ and $B^{[4]}$) is a very specific indicator of the physical accuracy of the FFs. To establish a baseline for MLIP performance on complex borosilicate glasses, we evaluated the predictive capabilities of two recent MACE foundation models, MatPES−PBE and MatPES-r^{2}SCAN,[68] which were trained on the Materials Potential Energy Surface (MatPES) datasets[69] labeled with DFT single-point calculations using PBE and r^{2}SCAN functionals on 400000 structures, respectively. Figure 5 shows the density and $B^{[4]}$%, for all compositions where they have been measured experimentally,[38] as calculated through MDs using the proposed melt-quench protocol in Figure 2. To ensure robust statistics, the melt-quench process was repeated several times, and the uncertainty in all physical properties was also represented.

The general trends of density vs glass composition (increasing amount of SiO_2) are in qualitative agreement with experiments for all XC functionals. However, there are quantitative differences among functionals. For example, densities obtained with MLIP-PBE show quite poor agreement, especially for compositions with SiO_2 / (SiO_2 + B_2O_3) ratio below 0.84. MLIP-PBEsol correctly reproduces the density as this SiO_2 ratio increases from 0 to 0.84, with a slight overestimation observed above this threshold. By contrast, MLIP-r^{2}SCAN, MLIP-PBE0, and MLIP-M06 underestimate the density when the ratio of SiO_2 is less than 0.68, while showing good agreement with experiments for higher compositions. Finally, MLIP-MN15 is the only model that tends to match the experimental density across all compositions. The two foundation models, MatPES−PBE and MatPES-r^{2}SCAN, underestimate the density across all compositions, with MatPES−PBE showing the worst accuracy. In contrast, MatPES-r^{2}SCAN predicts the density much more accurately, yielding results comparable to MLIP-PBE as the SiO_2 fraction increases. This improvement is especially clear for boron-rich compositions, where its accuracy is similar to that of MLIP-r^{2}SCAN.

From these comparisons we can derive three conclusions: first, XC functionals tend to have difficulty capturing the density, with the dispersion between various functionals being higher for boron-rich compositions. Second, if we focus on the overall accuracy of each functional across the glass composition range (Figure 5c), the errors for MLIP-PBEsol, MLIP-r^{2}SCAN, MLIP-PBE0, MLIP-M06, and MLIP-MN15 are always below 4%, with similar standard deviations, and lower than 2% in most cases—with MLIP-PBE performing much worse. Among the six scratch-trained models, MLIP-MN15 shows the lowest median percentage error, approximately 1%. Third, between the two foundation models, MatPES−PBE has a median percentage error of 10%, while MatPES-r^{2}SCAN has a lower percentage error of around 5%, which is twice that of MLIP-r^{2}SCAN, even though both models use the same functional.

This difference is primarily attributed to the fact that the reference Hamiltonians are different between our MLIPs and the foundation models in two aspects: first, the foundation

https://doi.org/10.1021/acs.jctc.6c01609
J. Chem. Theory Comput. 2026, 22, 10961−10976

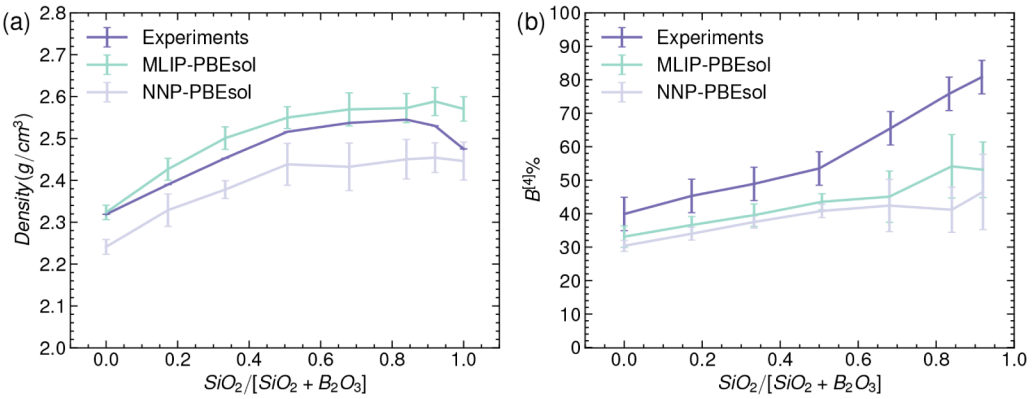


Figure 6. Comparison of (a) glass density and (b) $B^{[4]}$%, as a function of glass composition, as predicted by our model (MLIP-PBEsol) and Kayano et al.[36] (NNP-PBEsol) and compared to experimental data.[38]

models are trained on crystalline structures and may not fully capture the structural and chemical complexity of amorphous borosilicate glasses represented in our data sets; second, the foundation models have not been trained with the same dispersion-correction treatment as our MLIPs. A direct comparison has been made by fine-tuning the MatPES-r^{2}SCAN model on our data set, and although the model's accuracy is probably affected by the different dispersion treatment, the results show that the predicted density is located in the range calculated by our MLIP-r^{2}SCAN, but $B^{[4]}$% shows no improvement for the three key compositions (6B, 12B, and 24B) shown in Figure S21.

Focusing now on the local structure, we look at $B^{[4]}$% in Figure 5b, which increases monotonically as a function of SiO_2 content according to experiments. While this qualitative trend is captured by all XC functionals, we see that there is still a significant gap between experimental and computational values, with $B^{[4]}$% underestimated across the whole range of DFT functionals. This effect is particularly important when there are few boron atoms in the glass (high SiO_2 content)—although we note that these simulations have rather large uncertainties, due to the small number of boron atoms present. Of the different functionals, MLIP-PBEsol is the best-performing for all compositions (with about 20% error) when it comes to predicting the percentage of $B^{[4]}$. The scratch-trained MLIPs with the other four functionals (MLIP-PBE, MLIP-r^{2}SCAN, MLIP-PBE0, and MLIP-MN15) show essentially comparable accuracy. Interestingly, MLIP-M06 exhibits the largest error in the prediction of $B^{[4]}$% among the scratch-trained MLIPs, which is associated with the larger force errors for Na and O elements (see Table S4). This is also visible in the average performance of each functional across the glass composition range, depicted in Figure 5d. As for the foundation models, both underestimate $B^{[4]}$% across all compositions compared with experiments. MatPES−PBE shows similar accuracy to the six MLIPs trained from scratch for boron-rich compositions, but its accuracy begins to degrade when the SiO_2 fraction exceeds 0.5, resulting in a higher error than MLIP-PBE. By contrast, MatPES-r^{2}SCAN achieves an accuracy comparable to MLIP-r^{2}SCAN with a similar median relative error but higher standard deviation, as shown in Figure 5d.

Choice of Reference Exchange−Correlation Functional

The comparison of MLIP predictive capability for density and $B^{[4]}$% across compositions demonstrates that MLIP-PBEsol overall achieves the best accuracy for borosilicate glasses among the six scratch-trained MLIPs. It is worth highlighting that the density and boron coordination are influenced both by the MD simulation protocol (in particular, the quenching rate) and the accuracy of the MLIP force field. We first demonstrated the transferability of the proposed hybrid melt-quench protocol and evaluated the choice of switching temperature using an independent force field (a neural network potential developed by Kayano et al.[36] using DeePMD under PBEsol functional-based DFT data, referred to herein as NNP-PBEsol) at 1300 and 2000 K. We observed no distinct improvements in density and $B^{[4]}$% under the two different switching temperatures as shown in Figure S22. To investigate the influence of the quenching rate, we tested a more realistic rate (1 K/ps) for two representative compositions (12B and 24B, for which MLIPs show the largest prediction errors) using the best MLIP-PBEsol force field and following the proposed melt-quenching protocol. As shown in Figure S23, we did not observe a significant improvement in $B^{[4]}$% accuracy at 1 K/ps compared with 5 K/ps for the two compositions tested. This suggests that within the cooling-rate range explored here, the residual underestimation cannot be eliminated by slower quenching alone.

For this reason, and given that all of the MLIPs were trained to convergence and that the melt-quench protocol was identical in all cases, the overall accuracy was thus predominantly determined by the underlying DFT data, which in turn depend on the choice of XC functionals. Therefore, the PBEsol functional appears to be the best choice for the borosilicate glasses studied. That result contradicts the chemical intuition that higher levels of DFT, i.e., more expensive XC functionals, are expected to provide a better predictive ability. However, we want to highlight that PBEsol, which was specifically revised for solids, accurately reproduces the gradient expansion for slowly varying densities, and has been proven to perform remarkably well for bond lengths and lattice constants of densely packed solids and their surfaces.[42] The equilibrium properties are the basis of relevant physical properties such as density and bulk modulus for ionic and covalent solids, favoring a compact network structure, and this is true in particular for multicomponent oxide glasses as is the case here. In a specific comparison of functionals, the improvement of PBEsol over PBE for glass density was previously observed in sodium silicate glasses.[32] We therefore consider PBEsol to be our reference XC functional and MLIP-

https://doi.org/10.1021/acs.jctc.6c01609
J. Chem. Theory Comput. 2026, 22, 10961−10976

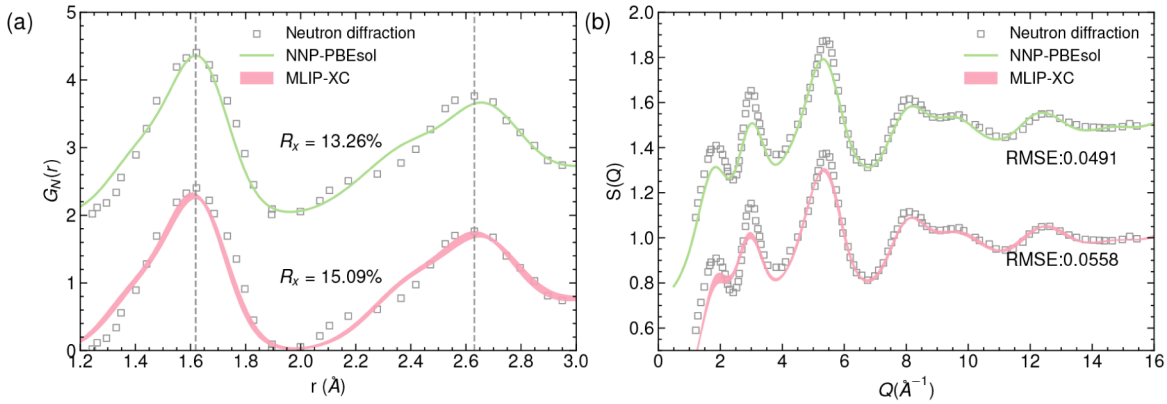


Figure 7. Experimental[40] and simulated (a) pair distribution functions, $G_N(r)$, and (b) structure factors, $S(Q)$, for the 10B glass computed with MLIP-XC in this work and NNP-PBEsol.[36] The pink area represents the uncertainty arising from the different XC functionals including PBEsol, PBE, r^{2}SCAN, PBE0, M06, and MN15. For the sake of comparison, we present the results of NNP-PBEsol and our scratch-trained MLIPs together. For clarity, the curves of NNP-PBEsol are vertically shifted by +2 and +0.5 for $G_N(r)$ and $S(Q)$, respectively.

PBEsol to be the most physically accurate of the models we have trained.

We note that, although the MLIP-PBEsol provided satisfactory density predictions, it still underestimates the $B^{[4]}$%—albeit to a lesser extent than other functionals tested. To check this specific feature, we wanted to validate the performance of our MLIP-PBEsol model against NNP-PBEsol,[36] the latest neural network force field for multicomponent oxide glasses in the literature. Kayano's model is also based on independently obtained DFT data at the PBEsol level, but uses a different MLIP architecture, and is therefore an interesting comparison with our own model. We use the NNP-PBEsol to generate glasses and determine their densities and $B^{[4]}$% and report the results in Figure 6. To quantify the discrepancy of predictions between the potentials and experiments, we computed the MAE for density and $B^{[4]}$%. In panel (a), we observe that the densities predicted by MLIP-PBEsol and NNP-PBEsol correctly reproduce the trend of density but exhibit different numerical values. The former reproduces density accurately for most compositions, with a very small MAE of 0.04 g/cm^3 compared to experiments, partly overestimating at low B_2O_3 content, while the latter basically underestimates density for all compositions with an MAE of 0.07 g/cm^3. Despite this difference, we find that both force fields underestimate $B^{[4]}$% in the same way (Figure 6b) across the composition range, with analogous MAEs of 14.93% and 19.56%, respectively.

The systematic underestimation of glass density in the NNP-PBEsol model can be simply explained by the lack of accounting for dispersion corrections in the methodology of Kayano et al.[36] Indeed, Pedone et al.[70] recently demonstrated that a DeePMD potential without D3 dispersion corrections for binary sodium silicate glasses underestimates the density by approximately 0.1 g/cm^3, in line with our observations of borosilicate systems. However, we also see that this difference in density is not the root cause of the limitations in the description of the balance between triangular BO_3 units and tetrahedral BO_4 units in borosilicate glasses. To the best of our understanding, this can be ascribed to one of two factors: either the experimental data may need to be confirmed or interpreted in a different manner, or the DFT calculations are missing some element of the description of the tetrahedral boron environment in a way that impacts all XC functionals tested in this work.

Impact of Exchange–Correlation Functional on Glass Structure

Pair Distribution Function and Structure Factor. To test the capabilities of extrapolation and generalization of our MLIPs, we applied them to a case outside our training data, with a totally new composition of borosilicate glass named "10B" (the detailed composition is shown in Table 1) for which experimental data are available. We focused on the prediction of structural properties: the pair distribution functions (PDFs, see eq S3) and their associated partial pair distribution functions (PPDFs), bond-angle distributions (BAD), as well as the structure factors ($S(Q)$, see eq S5) were calculated. These properties describe the short-range and medium-range order in the sodium–calcium borosilicate glass. We also calculated these properties for the NNP-PBEsol model.[36] To quantify the agreement between the MLIPs and experiments,[40] the R_x factor proposed by Wright[71] (see eq S2) and Root Mean Square Error (RMSE) were calculated.

Figure 7 shows the computed PDFs and $S(Q)$ of 10B glass, using the six MLIPs in this work and NNP-PBEsol, compared with experiments. In this figure, we plotted the results for all six MLIPs together shown as a pink band (labeled MLIP-XC), depicting both the average results and the uncertainty associated with the choice of the XC functional. We can see (panel a) an overall good agreement in PDF prediction for both MLIP-XC and NNP-PBEsol compared with neutron diffraction data, showing similar R_x of 15.09% and 13.26%, respectively. The narrowness of the pink band highlights that the differences between XC functionals in structural properties such as the PDF are very small, as is the difference between our work and the NNP-PBEsol model: the short-range order of the glass is consensual, in good agreement with experiments. The main features are the two peaks at around 1.62 Å and 2.62 Å: the first peak corresponds mainly to contributions by Si–O pairs, while the second one arises mostly from O–O pairs. However, a slight discrepancy between the MLIPs and experiments was observed at 1.2 to 1.4 Å, arising from B–O distances (see below for details). Another slight deviation can be found at 2.1 to 2.4 Å, representing Na–O distances: it is less prominent in NNP-PBEsol (and explains its somewhat lower R_x) because more binary and ternary components with sodium oxide were contained in their training data set.

https://doi.org/10.1021/acs.jctc.6c01609
J. Chem. Theory Comput. 2026, 22, 10961–10976

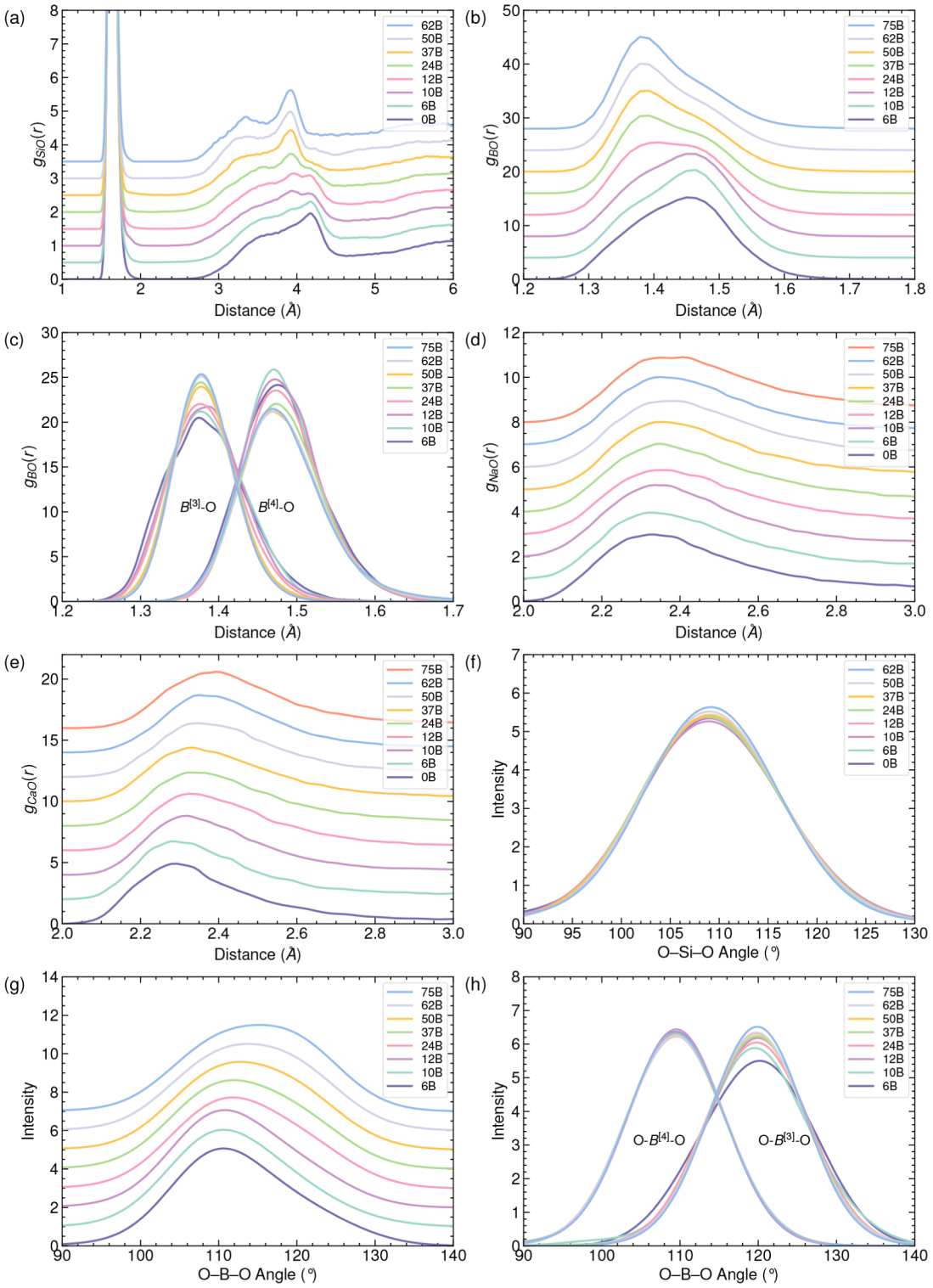


Figure 8. Partial pair distribution functions (PPDFs) and bond-angle distribution (BAD) of borosilicate glasses for different compositions (see Table 1): PPDFs—(a) Si–O, (b) B–O, (c) $B^{[3]}$–O and $B^{[4]}$–O, (d) Na–O, and (e) Ca–O; BAD—(f) O–Si–O, (g) O–B–O, and (h) O–$B^{[3]}$–O and O–$B^{[4]}$–O.

However, despite these small differences, the short-range structure is generally well reproduced.

The structure factor, as presented in Figure 7b, allows the assessment of MLIPs when it comes to medium-range order in the glass. The simulated $S(Q)$ of MLIP-XC and NNP-PBEsol are in line with experiments for both the position and shape of the peaks with a similar RMSE of about 0.05. Only the peaks at low Q values are somewhat underestimated in intensity. This slight underestimation is associated with insufficient accuracy in capturing the change in boron coordination, from BO_3 units to BO_4 units. In addition, we observed that MLIP-XC shows a slightly larger band in the first peak, indicating that there is some disagreement between XC functionals in this part of the plot: the choice of functional has some influence on the

https://doi.org/10.1021/acs.jctc.6c01609
J. Chem. Theory Comput. 2026, 22, 10961−10976

Table 3. Bond Distances And Angles Calculated Using the Six MLIPs of This Work and the NNP-PBEsol model[36]

	Si−O (Å)	$B^{[3]}$−O (Å)	$B^{[4]}$−O (Å)	Na−O (Å)	Ca−O (Å)	O−Si−O (°)	O−$B^{[3]}$−O (°)	O−$B^{[4]}$−O (°)
Experiments	1.640	1.380	1.470	2.300	2.350	109.00	120.00	109.00
MLIP-PBE	1.637	1.380	1.481	2.407	2.370	109.02	119.84	109.24
MLIP-PBEsol	1.639	1.378	1.473	2.388	2.355	109.05	119.98	109.52
MLIP-r^{2}SCAN	1.624	1.368	1.475	2.394	2.356	109.14	120.10	109.22
MLIP-PBE0	1.622	1.378	1.462	2.396	2.352	109.04	120.14	109.09
MLIP-M06	1.620	1.374	1.469	2.461	2.352	109.00	120.01	109.29
MLIP-MN15	1.621	1.365	1.465	2.474	2.388	108.87	120.05	109.37
NNP-PBEsol	1.634	1.379	1.476	2.352	2.305	109.04	119.95	109.32

medium-range order, which comes indirectly from the description of boron coordination.

Partial Pair Distribution Functions and Bond-Angle Distributions. To confirm the capability of the MLIPs to describe detailed atomic local environments, we then calculated the partial pair distribution functions for Si−O, B−O (deconvoluted into $B^{[3]}$−O and $B^{[4]}$−O), Na−O, and Ca−O, as well as the bond-angle distributions (BADs) for O−Si−O and O−B−O, across all glass compositions. For clarity, the results from MLIP-PBEsol are presented in Figure 8 and the results from other MLIPs are provided in Figures S24 to S29.

We first see (panel a) that glass composition has only a minute influence on the local environment of the Si atom, confirmed by an unchanging first coordination shell and small variations in peak positions in the second coordination shell as the composition changes. In contrast, the local environment of B atoms (panel b) is highly correlated to glass composition, characterized by the gradual shift of main peaks from around 1.40 Å to 1.46 Å as the B_2O_3 content decreases—in line with the transition of boron from 3- to 4-coordinated. To accurately assess the B−O distance, we deconvoluted the partial PDFs into $B^{[3]}$−O and $B^{[4]}$−O (panel c). The peaks of Na−O and Ca−O (panels d and e) are sensitive to composition, appearing in the range of 2.2 to 2.4 Å and gradually shifting toward larger distances as B_2O_3 is introduced. The trend is explained by the change in the role of these cations from network modifiers to charge compensators: in boron-rich glasses, Na^+ and Ca^{2+} cations preferentially compensate negatively charged boron atoms forming BO_4 environments, whereas when the boron content is lower, there is an excess of cations causing linkage breakage to create non-bridging oxygens. This is in line with other studies that find Na−O and Ca−O distances increase when acting as charge compensators rather than network modifiers.[40,72]

The angular distribution of oxygen around Si and B atoms is analyzed in the bond-angle distributions of Figure 8 (f−h). Again, the silicon environment (O−Si−O angle around 109°) is unaffected by glass compositions, while the O−B−O angles present a much broader distribution, with a clear bimodal nature, especially as boron content increases. A separation of the angle distributions around $B^{[3]}$ and $B^{[4]}$ (panel h) confirms the decomposition into tetrahedral O−$B^{[4]}$−O (around 109°) and trigonal O−$B^{[3]}$−O (around 120°). We further confirm that there is no continuum between the two, but an evolution of the two populations of boron atoms.

We summarize the observed bond lengths and angles in Table 3, where we report the values for all the XC functionals studied, as well as the NNP-PBEsol model (corresponding plots can be found in Figures S24 to S29), compared to experimental data from Michel et al.[40] There is overall very good agreement with experiments, with very minor influence of the XC functional. MLIPs trained with meta-GGAs and hybrid functionals give the same Si−O bond length at ∼1.620 Å, lower than ∼1.635 Å predicted by the GGA-based MLIPs, and slightly underestimate the Si−O bond length compared to experiments. The Na−O bond lengths predicted by MLIP-M06 and MLIP-MN15 are notably larger than those predicted by the other models and by experiments, which may be related to the larger force errors observed for Na and O in these two MLIPs.

CONCLUSIONS AND PERSPECTIVES

As we see the impact of AI methods being adopted in chemistry, one of the biggest revolutions in our field is the very fast adoption of machine-learned interatomic potentials; that is, neural networks for the description of interatomic interactions. The promise they make is clear and enticing: quantum chemical accuracy at the cost of a classical force field! For this reason, they are becoming widely used across chemistry and materials science. However, even if the neural networks have perfect accuracy and generalizability, they can only be as good as the reference data on which they have been trained. This is a fundamental principle that is well known in the AI field but is too often overlooked in practical applications. Because of the diversity of quantum chemistry methods, there is not actually a single ground truth for training these ML potentials.

In order to systematically study this question, we developed in this work MACE-based MLIPs for sodium−calcium borosilicate glasses and investigated the influence of several widely used XC DFT functionals, going from GGA to hybrid functionals, including PBE, PBEsol, r^{2}SCAN, PBE0, M06, and MN15, on the prediction of density and boron coordination as well as the structural description of the glass. To achieve this goal efficiently, we developed a hybrid melt-quench protocol integrating classical molecular dynamics at very high temperatures with MLIPs for quenching and equilibration to accelerate the molecular dynamics simulations without loss of accuracy in the final model.

Our results demonstrated that the influence of the exchange−correlation functional is not universal, but rather depends on the property being measured. While MLIPs based on most functionals are in good agreement for bulk properties such as glass density and local structure, we find that there are more important discrepancies between functionals in the description of the boron atomic environment and the medium-range order of the glass. Overall, for the prediction of physical properties, the MLIP based on PBEsol presented the highest accuracy for density and for $B^{[4]}$% among the six XC-functional-based MLIPs. However, our results also highlight that all MLIPs developed in this study, although trained on XC

https://doi.org/10.1021/acs.jctc.6c01609
J. Chem. Theory Comput. 2026, 22, 10961−10976

functionals at various theoretical levels, show a consistent mismatch with experiments in capturing the shift from $B^{[3]}$ to $B^{[4]}$. This suggests that the current XC functionals, even the more advanced ones, remain insufficiently accurate to fully describe the dynamic evolution of boron coordination in complex multicomponent glasses.

Based on the comparison across different theoretical levels, the prediction of $B^{[4]}$% is not simply related to the fraction of Hartree−Fock exchange (HFX). In our analysis, the predicted $B^{[4]}$% does not present a monotonic trend with increasing exchange contribution, spanning PBE (0% HFX), PBE0 (25% HFX), M06 (27% HFX), and MN15 (44% HFX): the predicted $B^{[4]}$% error decreases slightly from MLIP-PBE to MLIP-MN15, but MLIP-M06 shows the largest error. Thus, the fraction of HFX alone is insufficient to explain the differences in boron coordination between MLIP-XC and experiments. Other functional distinctions, such as the overall treatment of exchange and correlation and their functional forms and parameterizations, may also contribute to the underestimation of $B^{[4]}$%. Their relative contributions cannot be obtained from the current results. One possible contributing factor is the delocalization error, which may affect the relative stability of different boron coordination environments. Approximate DFT is known to suffer from the delocalization error, where the dominant Coulomb term pushes electrons apart,[73] which energetically favors the system whose electron density is spread out. In borosilicate glasses, this error potentially influences the relative stability of boron coordination because $B^{[3]}$ atoms forming planar BO_3 units have a relatively delocalized electron network compared to $B^{[4]}$ atoms with compact tetrahedral BO_4 units and the extra negative charge, thus favoring the formation of $B^{[3]}$ atoms and resulting in an underestimation of $B^{[4]}$%. The delocalization error can be corrected to some extent by increasing the fraction of HFX, although it cannot be completely eliminated.[74] The observed results in our work may partially match such an effect based on the reduction of relative error of predicted $B^{[4]}$% from MLIP-PBE to MLIP-MN15. However, the absence of a clear monotonic relationship between HFX fraction and $B^{[4]}$% underestimation indicates that the delocalization-error interpretation should be regarded as a possible hypothesis rather than the real origin of $B^{[4]}$% underestimation. A more direct assessment would require comparing the relative energy of BO_3 and BO_4 units using functionals with different treatments of delocalization error, for example, M06-HF[75] or long-range-corrected (LRC) hybrids (e.g., ωB97X-D).[76] Such an analysis is beyond the scope of the present work.

■ ASSOCIATED CONTENT

Data Availability Statement

All data and input scripts to support this study are publicly accessible on Zenodo at 10.5281/zenodo.21729081. This repository includes the training datasets, scratch-trained models, molecular dynamics trajectories following the hybrid melt-quench protocol, and representative scripts for DFT single-point calculations, MLIP training, LAMMPS simulation, and latent embedding analysis.

Supporting Information

The Supporting Information is available free of charge at https://pubs.acs.org/doi/10.1021/acs.jctc.6c01609.

DFT single-point calculations settings (Table S1); model parameters for six trained potentials (Table S2); statistics of computational time for six DFT exchange−correlation functionals (Table S3); mean square displacement of borosilicate glasses at 1300 K (Figure S1); evolution of loss function for MLIPs on training and validation data sets (Figures S2−S7); error metrics of energies and forces on the test set using MLIPs (Figures S8−S13); error metrics of forces on the *x*, *y*, and *z* axes for each composition using MLIP-M06 for the overall set (Figure S14); error metrics of forces on the *x*, *y*, and *z* axes for each composition using MLIP-MN15 for the overall set (Figure S15); two-dimensional PCA projection of transformed latent representations based on 100 DIRECT-sampled anchors extracted from MLIP-PBE (Figure S16); two-dimensional Principal Component Analysis (PCA) projections of transformed boron representations with boron coordination and B−O distances for all MLIPs (Figure S17); parity plot of the Mean Absolute Errors in energy differences (ΔE, in eV) across functional pairs on identical structural configurations (Figure S18); parity plot of the Mean Absolute Errors in Cartesian force differences (ΔF, in eV/Å) across functional pairs on identical structural configurations (Figure S19); parity plot of the Mean Absolute Errors in Cartesian force differences (ΔF, in eV/Å) across functional pairs on identical structural configurations without the contribution of Na (Figure S20); comparison of density and $B^{[4]}$% using fine-tuned MatPES-r^{2}SCAN and our MLIP-r^{2}SCAN (Figure S21); comparison of density and $B^{[4]}$% using NNP-PBEsol with switching temperatures at 1300 and 2000 K (Figure S22); influence of quenching rate on density and $B^{[4]}$% predicted using MLIP-PBEsol at 1 K/ps and 5 K/ps (Figure S23); equations including mean absolute error, the Wright equation (eq S2), root mean square error, pair distribution functions (eq S3), the partial structure factor (eq S4), and the structure factor (eq S5); PPDFs and BAD calculated by MLIP-PBE (Figure S24), MLIP-r^{2}SCAN (Figure S25), MLIP-PBE0 (Figure S26), MLIP-M06 (Figure S27), MLIP-MN15 (Figure S28), and NNP-PBEsol (Figure S29) (PDF)

■ AUTHOR INFORMATION

Corresponding Author

François-Xavier Coudert − *Chimie ParisTech, PSL University, CNRS, Institut de Recherche de Chimie Paris, Paris 75005, France;* orcid.org/0000-0001-5318-3910; Email: fx.coudert@chimieparistech.psl.eu

Authors

Fengming Shi − *Chimie ParisTech, PSL University, CNRS, Institut de Recherche de Chimie Paris, Paris 75005, France*

Luca Brugnoli − *Chimie ParisTech, PSL University, CNRS, Institut de Recherche de Chimie Paris, Paris 75005, France; Sorbonne Université, Muséum National d'Histoire Naturelle, UMR CNRS 7590, Institut de Minéralogie, de Physique des Matériaux et de Cosmochimie, IMPMC, Paris 75005, France*

Complete contact information is available at: https://pubs.acs.org/10.1021/acs.jctc.6c01609

Notes

The authors declare no competing financial interest.

■ ACKNOWLEDGMENTS

This work was supported by the Agence Nationale de la Recherche (project MATAREB, ANR-18-CE29-0009-01) and by the China Scholarship Council (CSC)—ParisTech 2024 program. Access to high-performance computing platforms was provided by GENCI (grant A0190807069).

■ REFERENCES

(1) Smedskjaer, M. M.; Youngman, R. E.; Mauro, J. C. Principles of Pyrex glass chemistry: Structure−property relationships. *Appl. Phys. A* **2014**, *116*, 491−504.
(2) Ellison, A.; Cornejo, I. A. Glass Substrates for Liquid Crystal Displays. *Int. J. Appl. Glass Sci.* **2010**, *1*, 87−103.
(3) Vienna, J. D.; Ryan, J. V.; Gin, S.; Inagaki, Y. Current Understanding and Remaining Challenges in Modeling Long-Term Degradation of Borosilicate Nuclear Waste Glasses. *Int. J. Appl. Glass Sci.* **2013**, *4*, 283−294.
(4) Varshneya, A. K.; Mauro, J. C. *Fundamentals of Inorganic Glasses*; Elsevier: Burlington, 2013.
(5) Sørensen, S. S.; Johra, H.; Mauro, J. C.; Bauchy, M.; Smedskjaer, M. M. Boron anomaly in the thermal conductivity of lithium borate glasses. *Phys. Rev. Mater.* **2019**, *3*, 075601.
(6) Pedone, A. Properties Calculations of Silica-Based Glasses by Atomistic Simulations Techniques: A Review. *J. Phys. Chem. C* **2009**, *113*, 20773−20784.
(7) *Molecular Dynamics Simulations of Disordered Materials: from Network Glasses to Phase-Change Memory Alloys*; Massobrio, C.; Du, J.; Bernasconi, M.; Salmon, P. S. Springer: Cham, 2015; Vol. *215*.
(8) Pedone, A.; Menziani, M. C.; Cormack, A. N. Dynamics of Fracture in Silica and Soda-Silicate Glasses: From Bulk Materials to Nanowires. *J. Phys. Chem. C* **2015**, *119*, 25499−25507.
(9) Deng, L.; Du, J. *Atomistic Simulations of Glasses*; John Wiley & Sons, Ltd, 2022; pp. 224−260.
(10) Pedone, A.; Bertani, M.; Brugnoli, L.; Pallini, A. Interatomic potentials for oxide glasses: Past, present, and future. *J. Non-Cryst. Solids: X* **2022**, *15*, 100115.
(11) Kieu, L.-H.; Delaye, J.-M.; Cormier, L.; Stolz, C. Development of empirical potentials for sodium borosilicate glass systems. *J. Non-Cryst. Solids* **2011**, *357*, 3313−3321.
(12) Deng, L.; Du, J. Development of boron oxide potentials for computer simulations of multicomponent oxide glasses. *J. Am. Ceram. Soc.* **2019**, *102*, 2482−2505.
(13) Wang, M.; Anoop Krishnan, N. M.; Wang, B.; Smedskjaer, M. M.; Mauro, J. C.; Bauchy, M. A new transferable interatomic potential for molecular dynamics simulations of borosilicate glasses. *J. Non-Cryst. Solids* **2018**, *498*, 294−304.
(14) Guillot, B.; Sator, N. A computer simulation study of natural silicate melts. Part I: Low pressure properties. *Geochim. Cosmochim. Acta* **2007**, *71*, 1249−1265.
(15) Coudert, F.-X. Failure to reproduce the results of "A new transferable interatomic potential for molecular dynamics simulations of borosilicate glasses". *J. Non-Cryst. Solids* **2023**, *615*, 122423.
(16) Sundararaman, S.; Huang, L.; Ispas, S.; Kob, W. New optimization scheme to obtain interaction potentials for oxide glasses. *J. Chem. Phys.* **2018**, *148*, 194504.
(17) Sundararaman, S.; Huang, L.; Ispas, S.; Kob, W. New interaction potentials for alkali and alkaline-earth aluminosilicate glasses. *J. Chem. Phys.* **2019**, *150*, 154505.
(18) Sundararaman, S.; Huang, L.; Ispas, S.; Kob, W. New interaction potentials for borate glasses with mixed network formers. *J. Chem. Phys.* **2020**, *152*, 104501.
(19) Tilocca, A.; de Leeuw, N. H.; Cormack, A. N. Shell-model molecular dynamics calculations of modified silicate glasses. *Phys. Rev. B* **2006**, *73*, 104209.
(20) Bertani, M.; Menziani, M. C.; Pedone, A. Improved empirical force field for multicomponent oxide glasses and crystals. *Phys. Rev. Mater.* **2021**, *5*, 045602.
(21) Bertani, M.; Pallini, A.; Cocchi, M.; Menziani, M. C.; Pedone, A. A new self-consistent empirical potential model for multicomponent borate and borosilicate glasses. *J. Am. Ceram. Soc.* **2022**, *105*, 7254−7271.
(22) Baral, K.; Li, A.; Ching, W.-Y. Ab Initio Modeling of Structure and Properties of Single and Mixed Alkali Silicate Glasses. *J. Phys. Chem. A* **2017**, *121*, 7697−7708.
(23) Li, W.; Zhao, X.; Liu, C.; Coudert, F.-X. Ab Initio Molecular Dynamics of CdSe Quantum-Dot-Doped Glasses. *J. Am. Chem. Soc.* **2020**, *142*, 3905−3912.
(24) Deng, L.; Du, J. Effects of system size and cooling rate on the structure and properties of sodium borosilicate glasses from molecular dynamics simulations. *J. Chem. Phys.* **2018**, *148*, 024504.
(25) Unke, O. T.; Chmiela, S.; Sauceda, H. E.; Gastegger, M.; Poltavsky, I.; Schütt, K. T.; Tkatchenko, A.; Müller, K.-R. Machine Learning Force Fields. *Chem. Rev.* **2021**, *121*, 10142−10186.
(26) Friederich, P.; Häse, F.; Proppe, J.; Aspuru-Guzik, A. Machine-learned potentials for next-Generation matter simulations. *Nat. Mater.* **2021**, *20*, 750−761.
(27) Ran, N.; Yin, L.; Qiu, W.; Liu, J. Recent advances in machine learning interatomic potentials for cross-scale computational simulation of materials. *Sci. China Mater.* **2024**, *67*, 1082−1100.
(28) Kobayashi, K.; Okumura, M.; Nakamura, H.; Itakura, M.; Machida, M.; Cooper, M. W. D. Machine learning molecular dynamics simulations toward exploration of high-temperature properties of nuclear fuel materials: Case study of thorium dioxide. *Sci. Rep.* **2022**, *12* (1), 9808.
(29) Erhard, L. C.; Rohrer, J.; Albe, K.; Deringer, V. L. A machine-learned interatomic potential for silica and its relation to empirical models. *Npj Comput. Mater.* **2022**, *8*, 90.
(30) Trillot, S.; Lam, J.; Ispas, S.; Kandy, A. K. A.; Tuckerman, M. E.; Tarrat, N.; Benoit, M. Elaboration of a neural-network interatomic potential for silica glass and melt. *Comput. Mater. Sci.* **2024**, *236*, 112848.
(31) Urata, S.; Bertani, M.; Pedone, A. Applications of machine-learning interatomic potentials for modeling ceramics, glass, and electrolytes: A review. *J. Am. Ceram. Soc.* **2024**, *107*, 7665−7691.
(32) Bertani, M.; Charpentier, T.; Faglioni, F.; Pedone, A. Accurate and Transferable Machine Learning Potential for Molecular Dynamics Simulation of Sodium Silicate Glasses. *J. Chem. Theory Comput.* **2024**, *20*, 1358−1370.
(33) Kato, T.; Lodesani, F.; Urata, S. Boron coordination and three-membered ring formation in sodium borate glasses: a machine-learning molecular dynamics study. *J. Am. Ceram. Soc.* **2024**, *107*, 2888−2900.
(34) Urata, S. Modeling Short-Range and Three-Membered Ring Structures in Lithium Borosilicate Glasses Using a Machine-Learning Potential. *J. Phys. Chem. C* **2022**, *126*, 21507−21517.
(35) Urata, S.; Tan, A. R.; Gómez-Bombarelli, R. Modifying ring structures in lithium borate glasses under compression: MD simulations using a machine-learning potential. *Phys. Rev. Mater.* **2024**, *8*, 033602.
(36) Kayano, R.; Inagaki, Y.; Matsubara, R.; Ishida, K.; Ohkubo, T. Development and Validation of Neural Network Potentials for Multicomponent Oxide Glasses. *J. Phys. Chem. C* **2024**, *128*, 17686−17702.
(37) Morawietz, T.; Singraber, A.; Dellago, C.; Behler, J. How van Der Waals Interactions Determine the Unique Properties of Water. *Proc. Nat. Acad. Sci.* **2016**, *113*, 8368−8373.
(38) Smedskjaer, M. M.; Mauro, J. C.; Youngman, R. E.; Hogue, C. L.; Potuzak, M.; Yue, Y. Topological Principles of Borosilicate Glass Chemistry. *J. Phys. Chem. B* **2011**, *115*, 12930−12946.
(39) Smedskjaer, M. M.; Mauro, J. C.; Yue, Y. Cation Diffusivity and the Mixed Network Former Effect in Borosilicate Glasses. *J. Phys. Chem. B* **2015**, *119*, 7106−7115.
(40) Michel, F.; Cormier, L.; Lombard, P.; Beuneu, B.; Galoisy, L.; Calas, G. Mechanisms of boron coordination change between borosilicate glasses and melts. *J. Non-Cryst. Solids* **2013**, *379*, 169−176.

https://doi.org/10.1021/acs.jctc.6c01609
J. Chem. Theory Comput. 2026, 22, 10961−10976

(41) Perdew, J. P.; Burke, K.; Ernzerhof, M. Generalized Gradient Approximation Made Simple. *Phys. Rev. Lett.* **1996**, *77*, 3865−3868.
(42) Perdew, J. P.; Ruzsinszky, A.; Csonka, G. I.; Vydrov, O. A.; Scuseria, G. E.; Constantin, L. A.; Zhou, X.; Burke, K. Restoring the density-gradient expansion for exchange in solids and surfaces. *Phys. Rev. Lett.* **2008**, *100*, 136406.
(43) Furness, J. W.; Kaplan, A. D.; Ning, J.; Perdew, J. P.; Sun, J. Accurate and Numerically Efficient r2SCAN Meta-Generalized Gradient Approximation. *J. Phys. Chem. Lett.* **2020**, *11*, 8208−8215.
(44) Adamo, C.; Barone, V. Toward reliable density functional methods without adjustable parameters: The PBE0 model. *J. Chem. Phys.* **1999**, *110*, 6158−6170.
(45) Zhao, Y.; Truhlar, D. G. The M06 Suite of Density Functionals for Main Group Thermochemistry, Thermochemical Kinetics, Noncovalent Interactions, Excited States, and Transition Elements: Two New Functionals and Systematic Testing of Four M06-class Functionals and 12 Other Functionals. *Theor. Chem. Acc.* **2008**, *120*, 215−241.
(46) Yu, H. S.; He, X.; Li, S. L.; Truhlar, D. G. MN15: A Kohn−Sham global-hybrid exchange−correlation density functional with broad accuracy for multi-reference and single-reference systems and noncovalent interactions. *Chem. Sci.* **2016**, *7*, 5032−5051.
(47) Kühne, T. D.; Iannuzzi, M.; Del Ben, M.; Rybkin, V. V.; Seewald, P.; Stein, F.; Laino, T.; Khaliullin, R. Z.; Schütt, O.; Schiffmann, F.; et al. CP2K: An electronic structure and molecular dynamics software package - Quickstep: Efficient and accurate electronic structure calculations. *J. Chem. Phys.* **2020**, *152* (19), 194103.
(48) Thompson, A. P.; Aktulga, H. M.; Berger, R.; Bolintineanu, D. S.; Brown, W. M.; Crozier, P. S.; in't Veld, P. J.; Kohlmeyer, A.; Moore, S. G.; Nguyen, T. D.; Shan, R.; Stevens, M. J.; Tranchida, J.; Trott, C.; Plimpton, S. J. LAMMPS - a flexible simulation tool for particle-based materials modeling at the atomic, meso, and continuum scales. *Comput. Phys. Commun.* **2022**, *271*, 108171.
(49) VandeVondele, J.; Krack, M.; Mohamed, F.; Parrinello, M.; Chassaing, T.; Hutter, J. Quickstep: Fast and accurate density functional calculations using a mixed Gaussian and plane waves approach. *Comput. Phys. Commun.* **2005**, *167*, 103−128.
(50) Lippert, G.; Hutter, J.; Parrinello, M. A hybrid Gaussian and plane wave density functional scheme. *Mol. Phys.* **1997**, *92*, 477−488.
(51) Goedecker, S.; Teter, M.; Hutter, J. Separable dual-space Gaussian pseudopotentials. *Phys. Rev. B* **1996**, *54*, 1703−1710.
(52) Hartwigsen, C.; Goedecker, S.; Hutter, J. Relativistic separable dual-space Gaussian Pseudopotentials from H to Rn. *Phys. Rev. B* **1998**, *58*, 3641−3662.
(53) Krack, M. Pseudopotentials for H to Kr optimized for gradient-corrected exchange-correlation functionals. *Theor. Chem. Acc.* **2005**, *114*, 145−152.
(54) Grimme, S. Semiempirical GGA-type density functional constructed with a long-range dispersion correction. *J. Comput. Chem.* **2006**, *27*, 1787−1799.
(55) Bussi, G.; Donadio, D.; Parrinello, M. Canonical sampling through velocity rescaling. *J. Chem. Phys.* **2007**, *126*, 014101.
(56) Sadigh, B.; Erhart, P.; Åberg, D.; Trave, A.; Schwegler, E.; Bude, J. First-Principles Calculations of the Urbach Tail in the Optical Absorption Spectra of Silica Glass. *Phys. Rev. Lett.* **2011**, *106*, 027401.
(57) Li, W.; Zhao, X.; Liu, C.; Coudert, F.-X. Influence of Glass Composition on the Luminescence Mechanisms of CdSe Quantum-Dot-Doped Glasses. *J. Phys. Chem. C* **2021**, *125*, 18916−18926.
(58) Brugnoli, L.; Miyatani, K.; Akaji, M.; Urata, S.; Pedone, A. New Atomistic Insights on the Chemical Mechanical Polishing of Silica Glass with Ceria Nanoparticles. *Langmuir* **2023**, *39*, 5527−5541.
(59) Yu, H. S.; He, X.; Truhlar, D. G. MN15-L: A New Local Exchange-Correlation Functional for Kohn−Sham Density Functional Theory with Broad Accuracy for Atoms, Molecules, and Solids. *J. Chem. Theory Comput.* **2016**, *12*, 1280−1293.
(60) Batatia, I.; Kovács, D. P.; Simm, G. N. C.; Ortner, C.; Csányi, G. MACE: Higher order equivariant message passing neural networks for fast and accurate force fields. In *Advances in neural information processing systems*; Curran Associates, Inc., 2022.
(61) Batatia, I.; Batzner, S.; Kovács, D. P. T.; Musaelian, A.; Simm, G. N. C.; Drautz, R.; Ortner, C.; Kozinsky, B.; Csányi, G. The design space of E(3)-equivariant atom-centered interatomic potentials. *Nat. Mach. Intell.* **2025**, *7*, 56−67.
(62) Urata, S.; Lodesani, F. Certification of Boroxol Ring Population in Vitreous B_2O_3 Glass Using Theoretical Simulations. *Materialia* **2025**, *42*, 102474.
(63) Meher, D.; Avula, N. V. S.; Balasubramanian, S. Slowly Quenched, High Pressure Glassy B_2O_3 at DFT Accuracy. *J. Chem. Phys.* **2025**, *162* (4), 044503.
(64) Li, Z.; Walsh, A. Platonic Representation of Foundation Machine Learning Interatomic Potentials. *Nat. Mach. Intell.* **2026**, *8*, 830−840.
(65) Qi, J.; Ko, T. W.; Wood, B. C.; Pham, T. A.; Ong, S. P. Robust Training of Machine Learning Interatomic Potentials with Dimensionality Reduction and Stratified Sampling. *Npj Comput. Mater.* **2024**, *10*, 43.
(66) Schönemann, P. H. A Generalized Solution of the Orthogonal Procrustes Problem. *Psychometrika* **1966**, *31*, 1−10.
(67) Peyré, G.; Cuturi, M.Computational Optimal Transport. *arXiv***2020**, arXiv:1803.00567.
(68) Batatia, I.; Benner, P.; Chiang, Y.; Elena, A. M.; Kovács, D. P.; Riebesell, J.; Advincula, X. R.; Asta, M.; Avaylon, M.; Baldwin, W. J.; et al. A Foundation Model for Atomistic Materials Chemistry. *J. Chem. Phys.* **2025**, *163* (18), 184110.
(69) Kaplan, A. D.; Liu, R.; Qi, J.; Ko, T. W.; Deng, B.; Riebesell, J.; Ceder, G.; Persson, K. A.; Ong, S. P. A Foundational Potential Energy Surface Dataset for Materials. *arXiv* **2025**, **arXiv:2503.04070**.
(70) Pedone, A.; Bertani, M.; Benassi, M. Revisiting Machine Learning Potentials for Silicate Glasses: The Missing Role of Dispersion Interactions. *J. Chem. Theory Comput.* **2025**, *21*, 4769−4778.
(71) Wright, A. C. The comparison of molecular dynamics simulations with diffraction experiments. *J. Non-Cryst. Solids* **1993**, *159*, 264−268.
(72) Bauchy, M.; Micoulaut, M. Atomic scale foundation of temperature-dependent bonding constraints in network glasses and liquids. *J. Non-Cryst. Solids* **2011**, *357*, 2530−2537.
(73) Cohen, A. J.; Mori-Sánchez, P.; Yang, W. Insights into Current Limitations of Density Functional Theory. *Science* **2008**, *321*, 792−794.
(74) Bryenton, K. R.; Adeleke, A. A.; Dale, S. G.; Johnson, E. R. Delocalization Error: The Greatest Outstanding Challenge in Density-functional Theory. *WIREs Comput. Mol. Sci.* **2023**, *13* (2), No. e1631.
(75) Zhao, Y.; Truhlar, D. G. Density Functional for Spectroscopy: No Long-Range Self-Interaction Error, Good Performance for Rydberg and Charge-Transfer States, and Better Performance on Average than B3LYP for Ground States. *J. Phys. Chem. A* **2006**, *110*, 13126−13130.
(76) Chai, J.-D.; Head-Gordon, M. Long-Range Corrected Hybrid Density Functionals with Damped Atom−Atom Dispersion Corrections. *Phys. Chem. Chem. Phys.* **2008**, *10*, 6615−6620.

https://doi.org/10.1021/acs.jctc.6c01609
J. Chem. Theory Comput. 2026, 22, 10961−10976